

LA-UR- 07-08226

Approved for public release;  
distribution is unlimited.

<i>Title:</i>	Assessment of Corrosion-Based Failure in Stainless Steel Containers Used for the Long-Term Storage of Plutonium-Based Salts
<i>Author(s):</i>	R.S. Lillard, D.G. Kolman, M.A. Hill, M.B. Prime, D.K. Veirs, L.A. Worl, and P. Zapp
<i>Intended for:</i>	Corrosion, 65(3), 175-186



Los Alamos National Laboratory, an affirmative action/equal opportunity employer, is operated by the Los Alamos National Security, LLC for the National Nuclear Security Administration of the U.S. Department of Energy under contract DE-AC52-06NA25396. By acceptance of this article, the publisher recognizes that the U.S. Government retains a nonexclusive, royalty-free license to publish or reproduce the published form of this contribution, or to allow others to do so, for U.S. Government purposes. Los Alamos National Laboratory requests that the publisher identify this article as work performed under the auspices of the U.S. Department of Energy. Los Alamos National Laboratory strongly supports academic freedom and a researcher's right to publish; as an institution, however, the Laboratory does not endorse the viewpoint of a publication or guarantee its technical correctness.

ASSESSMENT OF CORROSION BASED FAILURE IN STAINLESS  
STEEL CONTAINERS USED FOR THE LONG-TERM STORAGE OF  
PLUTONIUM BASED SALTS

RS Lillard, DG Kolman, MA Hill, MB Prime, DK Veirs, LA Worl  
Materials Corrosion and Environmental Effects Lab  
Materials Science and Technology Division, MST-6  
Los Alamos National Laboratory  
Los Alamos, New Mexico 87545

P Zapp

Savannah River National Laboratory  
Washington Savannah River Co.  
Savannah River Site  
Aiken, SC 29808

**ABSTRACT**

This paper summarizes our efforts to assess corrosion related failure in stainless steel long-term storage containers baring plutonium oxides and electrorefining salts. Pitting corrosion of the internal can wall is believed to occur when these salt particles deliquesce forming the electrolyte necessary for corrosion-electrochemistry. Extrapolation of pit depths from coupon studies using GEV statistics found that the probability of a through-wall corrosion pit is finite; the maximum pit depth after 50 yrs. would be on the order of 1.7 mm where as the container wall is only 1.6 mm thick. To assess susceptibility to environmental cracking fracture toughness ( $J_{1c}$ ) experiments data from CT experiments were used in conjunction with a J-integral diagram constructed using the GE/EPRI method for linear elastic-plastic materials. As a part of this analysis the residual stress associated with the weld was measured using the laser contour method. The hoop stress in the weld region was found to be on the order of 135 MPa-180MPa. Assuming that the axial stress that results from the weld is equal to one half of the hoop stress ( $\sigma_{ax} = \sigma_h/2$ ) and our laboratory measurement of  $J_{1c}$  is accurate, one would conclude there is sufficient energy in associated with the weld to propagate a crack in the 3013 container.

## INTRODUCTION

The US Department of Energy 3013 Standard(1) covers the safe interim storage of a variety of Pu materials throughout the Complex for 50 years and beyond. Because these materials originate from a variety of environmental management and materials disposition programs, the range of materials is extensive, ranging from nearly pure  $\text{PuO}_2$  to impure Pu salts ( $\text{PuO}_2$  mixed with NaCl, KCl,  $\text{MgCl}_2$  and other metal halides). The Standard requires that, prior to storage, the materials be treated in an oxidizing atmosphere for a minimum of 2 h at  $950^\circ\text{C}$  (or  $750^\circ\text{C}$  equivalent for some classes of materials) and that the material subsequently contains less than 0.5 wt.% of what?. This stabilization treatment is required to reduce the reactivity of the materials such that gas generation and subsequent pressurization is not a problem. Specifically, this treatment is designed to reduce the volatile species content, especially water. Although this treatment tends to reduce the corrosivity of the stored material, the container materials will still be exposed to ionizing radiation, elevated temperatures, embrittling and/or alloying agents (e.g., Ga and Pu), chloride-containing compounds, and a limited quantity of moisture. In addition, containers will incorporate welds that may have heterogeneous compositions due to solute segregation and that may retain significant residual stress.

The goal of this program is to develop a methodology for predicting lifetime expectancies for 3013 as it relates to corrosion induced failure. As such, we have identified two potential, and related, phenomena as the most likely corrosion related failure mechanisms: pitting corrosion and environmental induced cracking. In this paper we will first present an overview of our pitting corrosion and environmentally assisted cracking studies including both laboratory experiments and surveillance data. We will then propose a method for extrapolating these data in space and time to assess container lifetimes.

Design Specifications for Storage Containers of Plutonium Baring  
Materials:  
The 3013 Standard

Container materials. The Standard dictates that storage containers be composed of an outer and inner container. While the use of any 300-series stainless steel for the inner and outer containers is allowed by the storage standard, the outer container (which is considered to be the pressure vessel) is composed of type 316 L stainless steel (SS). The outer container is specified to be 119 mm in diameter (ID), 246 mm tall, and have a wall thickness of 3.00 mm and contain one of two types of closure welds, either a laser weld or a gas tungsten arc welds (GTAW). The outer container is designed to withstand a pressurization of 21 MPa (defect free surface). Current materials for inner containers include both SS 304L and SS 316. While no specific container design is called for in the Standard for inner container, containers are expected to incorporate geometries similar to the following: The inner container is expected to be 114 mm in diameter (ID), 221 mm tall, and have a wall thickness of 0.889 mm. and contain two welds (GTAW or Laser). The inner container is designed to withstand a pressurization of 4.8 MPa (defect free).

Plutonium Based Materials. The containers are designed to store a mixture of Pu-oxide and electrorefining salts (ER salts) stored. The typically are composed of 95% by weight of an equimolar mixture of sodium chloride and potassium chloride with 5% by weight of anhydrous magnesium chloride. The  $\text{PuO}_2$ /salt ratio may be as large as 20 weight percent salt. Because stored materials will not necessarily be homogeneous, local concentrations may approach that of pure salts.

Water concentration. Stored materials may contain up to 0.5 wt.% water and assuming an upper storage limit of 5 kg, 25 g of water may be present. With respect to corrosion and water content there are two concerns, thermal transients can result in desorption and/or migration of this water. Under certain conditions, the gaseous water may condense on the container walls that are colder than the stored radioactive material. In addition, as discussed below hydrated salts may act as the electrolyte necessary for electrochemistry.

Temperature. The storage standard sets a 250°C temperature limit for storage containers regardless of normal, off-normal, or transportation conditions. Thermal modeling [19] and experimental measurement indicate that the wall temperature of an isolated container in ambient conditions would not approach 250°C. Practical experience at SRS indicates that actual temperatures will be below 100°C. Measurements (4.4 kg of 87% Pu (9 W) in a 24°C environment) revealed that convenience container wall temperatures ranged between 30°C and 89°C, depending on thermocouple placement and fill gas. Inner container wall temperatures ranged between 29°C and 41°C, and outer container wall temperatures were between 29°C and 37°C.

Radiation flux. The radiation flux will vary between containers. Containers will contain between 30 and 100 wt.% Pu. The total stored mass and the presence of other compounds that produce and absorb ionizing radiation will vary between containers. Thus, the range of ionizing radiation flux is expected to be quite large. For example, the neutron radiation from  $^{239}\text{Pu}$  metal is approximately 100,000 times less than that from  $^{239}\text{PuF}_4$  ( $3.0 \times 10^{-2}$  neutrons/g·s vs.  $4.3 \times 10^3$  neutron/g·s). Assuming that the container contains 100% of  $^{238}\text{PuF}_4$  (the most prolific stored neutron source), a neutron flux of  $4 \times 10^{20}$  neutrons/m<sup>2</sup> 50-year is calculated for the container material. Neutron energies vary from fission to fission but the average neutron energy from  $^{239}\text{Pu}$  following fission is 2 MeV. Calculations of radiation damage are more complex because of the self-absorption of Pu and its compounds. Using a variety of assumptions, the container wall will experience a fluence of approximately  $10^{19}$  a particles/m<sup>2</sup> over a 50-year period for  $^{239}\text{Pu}$ . These particles will vary in energy from 5.1 to 0 MeV.  $^{238}\text{Pu}$  can generate an alpha fluence that is approximately 300 times larger.  $^{239}\text{Pu}$  exhibits no  $\beta$  decay and its  $\gamma$  emission is relatively insignificant. In addition to these isotopes stored materials may include up to 2.8%  $^{241}\text{Am}$  ( $\gamma$ ), 1.44 %  $^{241}\text{Pu}$  ( $\beta$ ).

## PITTING CORROSION

### Introduction

Here we consider the pitting corrosion of the inner can walls as a case of atmospheric corrosion with the distinction that the "ambient air" is the environment inside the sealed container. The environment of the inner container consists of an oxide-salt mixture with up to 0.5 wt% H<sub>2</sub>O in steady state with a surrounding, headspace, gas. Initially, the gas is inert (He), however, with time increases in hydrogen and oxygen occur owing to water radiolysis as described above. The water primarily resides in the salt itself as waters of hydration or deliquesced material. Corrosion is thought to occur when an oxide-salt particle on the container wall deliquesces resulting in the electrolyte necessary for electrochemistry. To understand the development of this surface chemistry one must first consider the deliquescence and efflorescence of salts. Deliquescence is defined as the liquefaction of a salt by the attraction and absorption of moisture from the atmosphere. The deliquescence point (DP) is the relative humidity (RH) at which deliquescence occurs, and is a function of temperature and salt composition. As the DP will always be below the dew point we have ruled out condensation as the primary mechanism for electrolyte formation though we recognize that it may occur to a lesser extent. Below the DP water adsorbs onto the crystalline salt as waters of hydration. At the DP a step increase in water concentration occurs (for example, from 6 waters of hydration to an equivalent of 9) as the salt liquefies. Above the DP water absorption results in dilution (Figure 1). The process by which a deliquesced salt becomes crystalline is known as efflorescence, and the efflorescence point (EP) is the RH at which this occurs. Note in Figure 1 that the EP occurs at a RH that is well below the DP. A natural corollary to this discussion is that the composition of the deliquesced material controls the relative humidity inside the container.

The electrorefining salts (ER salts) stored in 3013 typically are composed of 95% by weight of an equimolar mixture of sodium chloride and potassium chloride with 5% by weight of anhydrous magnesium chloride.(2) Calcium chlorides have also been detected. Moisture sorption by plutonium oxide materials containing ER salts is a complex process with known mechanisms including surface adsorption of approximately a monolayer, formation of hydrated salts, and deliquescence. X-ray diffraction (XRD) of mixtures of calcined (heated) KCl, NaCl, and MgCl<sub>2</sub> have identified KMgCl<sub>3</sub>, K<sub>2</sub>MgCl<sub>4</sub>, and K<sub>3</sub>NaMgCl<sub>6</sub> as compounds that may be present in ER salts.(3) The only reported hydrate of these salts is KMgCl<sub>3</sub>·6H<sub>2</sub>O (carnallite). XRD measurements confirm that the more complex K<sub>2</sub>MgCl<sub>4</sub>, K<sub>3</sub>NaMgCl<sub>6</sub>, and ER simulant phase separate at low RH into KMgCl<sub>3</sub>·6H<sub>2</sub>O and the respective alkali halides. Carnallite further phase separates upon deliquescence to MgCl<sub>2</sub>·6H<sub>2</sub>O (bischofite) and carnallite. The deliquescent RHs for bischofite and carnallite at 25°C are 33% and 59%, and they decrease to 24% and 48% at 90°C.(4-6) As it relates to the corrosion of these containers, the RH of the glove box at the time of loading the ER salt into the can is especially important (so called dry glove boxes vs. ambient glove boxes). For ER salt exposed to RHs greater than 33% we conclude that deliquescence of oxide-salt particles on the container wall will provide the electrolyte necessary for corrosion electrochemistry.

## Experimental Methods

Exposure studies The final composition of the Pu oxide / ER salt used in these exposure studies is presented in Table 1. This material was generated by calcining a blend of materials to simulate the ER salts resulting from the Pu pyrochemical process. In this process material was calcined in two stages (600° C then 950° C). The moisture content of this material was determined to be 0.20 wt %. Screening found that the calcined material contained 38.8% of the mass was larger than 40 mesh screen (chunks) and the remain 61.2% considered powder. This material was placed in stainless steel 304L containers with five milliliter internal volume scaled to 1/500th of 3013 storage can. The inner container is constructed from 0.500 inch OD tubing at a thickness of 0.117 inch. These containers served as our coupons for the exposure studies. Here we will discuss the result from only one of these containers designated ARF 223-SSR110. After loading the containers with the Pu-oxide/salt material and backfilling with He gas they were placed in temperature-controlled blocks that could be heated to a temperature of 50 C, similar to that seen in the full-scale containers. The container pressure and temperature are recorded every fifteen minutes. Pressure accuracy is  $\pm 1.0$  kPa with repeatability of  $\pm 0.1$  kPa and temperature accuracy is  $\pm 1.7$  °C with repeatability of  $\pm 0.1$  °C. Gas chromatography (HP 5890) was the primary analytical tool for quantifying the gas composition in the headspace of the small-scale containers. Mass spectrometry could be used if there are unidentified peaks in the gas chromatogram. The total gas volume sampled during the course of the surveillance is limited to 10% of the total head space volume by limiting the number of gas samples taken. Table 2 shows the pressure data for ARF 223-SSR110 over the course of the exposure period. As seen in this table the primary radiolysis products were CO<CO2<H2 while the residual O2 in the container was consumed.

The exposure period for the container was approximately 170 days. Subsequent to the exposure, samples were analyzed for pitting damage by imaging them in a scanning electron microscope (SEM). Graphical analysis software was employed to determine pit sizes. For round pits, pit depths were equal to the pit radius. For other pits, an equivalent pit radius was calculated. In this method the pit surface area was measured and an equivalent radius (depth) was determined assuming a hemispherical geometry.

Statistical analysis of data In a previous publication we reported on several laboratory methods for accelerated testing and evaluated and their ability to access pitting damage during immersion in environments that simulate HLRW.(7) Specifically, we examined and compared corrosion current density, open circuit potential (OCP), metastable pitting data, and electrochemical noise (EN) data. In that work generalized extreme value (GEV) statistics was used to evaluate the distribution of current transient generated by EN experiments. Given the three classical extreme value distributions (Type I: Gumbel, Type II: Frechet and, Type III: Weibull), in the generalized form (GEV), all three distributions are considered in the cumulative distribution function (CDF):

$$GEV(u, \alpha, k) = \exp \left\{ - \left[ 1 - k(x - u) / \alpha \right]^{1/k} \right\} \quad kx < \alpha + uk \quad (1)$$

where:  $x$  represents the pit depth. The advantage of GEV over using an individual extreme value model (Type I, II, or III) is that it eliminates the need to determine which of the three models is most appropriate prior to fitting the data. In Eq. 1 the fitting parameters retain their usual meaning:  $u$  is a location parameter,  $\alpha$  is a scale parameter, and  $k$  is a shape parameter.

Analysis of pit depths from the exposure studies described above were conducted using the GEV software developed by Laycock *et al.* (8) was used to model the current transient and pit depth data to obtain values for  $\alpha$ ,  $u$ , and  $k$  (Eq. 1). The software was written using visual Fortran and fits the three parameter generalized extreme value distribution to a set of maxima. The probability weighted moment method, or Menon's method, was used to calculate initial estimates. This was followed by iteration to find the maximum likelihood estimates (MLE). Similar Fortran code that uses only the MLE for fitting data is available, see Hosking. (9)<sup>1</sup> MLE has the advantage of providing a variance/co-variance matrix while Menon's method is more applicable to small sample sizes. However, difficulties arise using the MLE method when  $k < -1$  as the likelihood function tends to  $\infty$ . Although maximum likelihood estimators are obtainable when  $-1 < k < -0.5$ , the estimator does not have standard asymptotic properties.<sup>15</sup> When  $k > -0.5$ , maximum likelihood estimators are asymptotically normal. Distributions with a very short bounded upper tail are associated with  $k \leq -0.5$ .

## Results and Discussion

To obtain a distribution of pit sizes on the container wall it was necessary to remove corrosion product from the surface of the container as it obscured the size of the underlying pits. This was done with a soft nylon brush. SEM micrographs of the same area taken before and after removal of corrosion product are presented in Fig. 3a and 3b. The "before" figure also shows many small domed features which after cleaning reveal the smallest of corrosion some of which were not removed by the cleaning process. In addition, SEM examination of the interior of the container found the corrosion pits to be shallow, a radius to diameter ration on the order of 1/4. In comparison, hemispherical pits would have a radius to diameter ratio of 1/2. A distribution of pit depths for a sample region in the headspace of ARF 223-SSR110 is presented in the form of a histogram in Fig. 2. The threshold pit depth used to collect these data was 12  $\mu\text{m}$ . Similar analysis was also carried out for the oxide contact region and the resulting histogram is shown in Figure 4.

The distribution of pits observed on the can interior was fit using a three-parameter GEV routine using a probability weighted moments method (Fig. 5). A full discussion of our method has been presented elsewhere. (7) The resulting fitting parameters for the head space and contact region are presented in Table 3. These parameters were then

<sup>1</sup> Currently available online at: [www.research.ibm.com/people/h/hosking/](http://www.research.ibm.com/people/h/hosking/)

used to project in time the maximum pit depths that might be observed in an actual 3013 container using the relationship:

$$\mu_{\max} = \left(u + \alpha/k\right)^b - \left(\alpha M^{-k} t^b\right) \Gamma(1+k) \quad (2)$$

where M is the ratio of the headspace area in an actual 3013 container (296 cm<sup>2</sup>) to the area in the headspace of ARF 223-SSR110 (3.68 cm<sup>2</sup>), t is time and b is a constant assumed to be 0.5. As seen in Fig. 6, the likelihood of a through wall penetration in the headspace over a 50 year lifetime of a 3013 container where similar corrosion processes are occurring is low, GEV analysis predicts that the maximum pit depth after a benchmark storage time of 50 yrs. would be approximately 264 μm while the can wall is approximately 1.67x10<sup>3</sup> μm thick. The error in this projection is calculated from the variance co-variance matrix as described previously.(7) For the contact region, however, the likelihood of a through-wall penetration is high. Extrapolation of our data indicates that the maximum pit depth after 50 years of exposure will be on the order of 1.8 mm. However, if our theory for the mechanism is correct, that is salt deliquescence, the water in the electrolyte is not limitless and may dry out owing to the hydrolysis of cations well before the corrosion pits are capable of penetrating the can wall. This rationale may well explain the hard corrosion covers seen in the SEM micrographs above.

## ENVIRONMENTALLY ASSISTED CRACKING AND FRACTURE TOUGHNESS

### Introduction

Given the limited availability of electrolyte described above, one might wrongly conclude that environmentally assisted cracking (EAC) would not be a problem in the 3013 container. Coupon studies of SS 316L (teardrop samples) exposed to an ER salt environment have shown that large cracks can form and propagate in these salts, especially near welds (Fig. 7). To assess the susceptibility of container materials to EAC we have chosen two approaches. In this section we describe the results of fracture toughness measurements. In the subsequent section we will show how to use these data to assess EAC susceptibility for flaws in a container with our geometry.

The most common fracture toughness test method is the ASTM method for measuring plane strain fracture toughness(10) and corresponding  $K_{Ic}$  that can be determined for material/environment combinations from this method. As the title indicates, the data analysis assumes that the strain (deformation) is limited to the plane of the advancing crack front. For most structural materials, this assumption is not valid. For example, austenitic steels undergo a substantial amount of plastic deformation and, as such, valid  $K_{Ic}$  testing would require sample thicknesses on the order of several cm. Alternately, J-integral analysis can be used which is also described in the same ASTM E1820. The test method is identical to that for the plane strain test, however, the analysis of the data accounts for plastic deformation.  $J_0$  is the crack tip energy release rate and can be calculated from the area under the load displacement curve. If certain conditions are met, the measured fracture toughness  $J_0$  is referred to as  $J_{Ic}$ . Like  $K_{Ic}$ ,  $J_{Ic}$  is considered a material property and can be easily extrapolated to other length scales. In this section we describe our measurement of

$J_{1c}$  using compact tension (CT) specimens and the method described in ASTM E1820-01.

## Review of SS 316 EAC Literature

There has been a wealth of publication in the field of environment-induced cracking of austenitic stainless steels in chloride environment. A recent review by Kolman has summarized much of the work as it pertains to the 3013 environment.(11) In general, there are two main theories that attempt to describe the fundamental processes that result in environmental fracture of austenitic stainless steels in chloride: the slip-dissolution model and the film-induced cleavage model.(12) In the slip-dissolution model, the crack walls remain passive while active dissolution at the crack front is maintained by the continual emergence of slip steps. In the film-induced cleavage model, cleavage occurs in a brittle, dealloyed metallic layer at the crack tip that is believed to be covered by a nanoporous oxide layer. Though these models are strikingly different, the kinetics of each mechanism are related to the crack tip chemistry. Therefore, in our investigation it will be imperative to examine the influence of crack tip chemistry on  $K_{1c}$ . While there has been a great deal of literature describing the fundamental processes of environment-induced cracking of austenitic stainless steels, little fracture toughness data for SS 316 in chloride exists.

Fracture toughness data for SS 316L is primarily limited to reactor applications. In that case, the primary concern is radiation hardening of the material. This is of some interest to 3013 as the container will see some neutron dose, though the levels may be quite low the anticipated storage time is long. In addition, the literature provides reference non-irradiated air fracture toughness values that will be used for comparison with the data collected in this program. It has been shown by Odette and Maziasz for neutron irradiation, LWR conditions (288° C), that the fracture toughness of SS 316L ( $K_{1c}$ , that is,  $K_{1c}$  calculated from  $J_{1c}$ ) decreases from a non-irradiated values of on the order of 200-300 MPam<sup>1/2</sup> after a dose of approximately 0.5 dpa (displacements per atom).(13) For a dose of 2 dpa, fracture toughness values were approximately half of the air measured values and continue to decrease with increasing dose. Similar data have been reported by Maloy *et al.*(14) for neutron dose in accelerator conditions (200° C) and Matsui *et al.*(15) for neutron dose in fusion reactor conditions (20° C). These data in combination with calculations of neutron dose over the 3013 container lifetime will be used to determine whether or not the 3013 fracture toughness data generated in this program will need to be adjusted for radiation induced hardening.

## Experimental Methods

Drawings of the CT(J) specimens used to investigate environment-induced cracking in 3013 containers is shown in Fig. 8. As seen in this figure the specimen is designed to accommodate a load-line extensometer (clip-gauge), direct current potential drop (DCPD) current leads, and DCPD voltage sensing leads. Critical ASTM dimensions in this design include  $W= 25$  cm,  $b= 12.5$  mm, and  $2H= 30.0$  mm. While the specimen thickness ( $b$ ) is approximately 15% less than the minimum value for SS 316  $J_{1c}$ , it has been shown for SS 316 that  $J_0$

changes vary little for sample thickness between 10 and 25 mm. Although it has been reported that there is little difference in fracture toughness data with sample orientation, samples will be machined in the T-S and L-T directions where L is the rolling direction. The L-T sample is a low toughness orientation as the crack in this geometry propagates in the rolling direction. This geometry represents a fracture that initiates at a 3013 weld and propagates perpendicular to the weld into the base material. The T-S sample geometry represents a crack that initiates at a flaw, such as a corrosion pit, and propagates through the 3013 wall. Here all data reported are from samples oriented in the L-T direction

Data were collected using a horizontal mounted MTS servo-hydraulic test frame and the TestStar II software. Prior to J-integral testing, samples were fatigue pre-cracked using a load of 5100 N applied at a frequency of 5 Hz. The final pre-crack length was approximately 3 mm that required  $3.0 \times 10^4$  cycles. The rising load displacement (RLD) portion of the experiment was done under load control at a rate of 0.001 mm/s. Crack mouth opening displacement was measured with an extensometer. Crack growth was measured using the DCPD method. Here a current of approximately 2.5 amps produced a potential drop of approximately 0.5 mV. This signal was amplified such that  $1 \times 10^{-6}$  V in potential drop was easily resolved. All experiments were carried out in an environmentally controlled chamber at 27° C. Data were analyzed using section A2.4.2.2 J of ASTM E 1820. (10)

Fracture toughness measurements were conducted in air, de-ionized water, or a simulated crack tip solution as noted. In this investigation, the simulated crack tip solution consisted of 0.75M  $MgCl_2/0.5M NaCl$  (2M  $Cl^-$ ). This solution was chosen to represent the high  $MgCl_2$  content believed to be in some of the 3013 containers. Future investigations will examine the influence of pH,  $Cl^-$  concentration, and temperature.

## Results and Discussion

Typical rising load displacement data are presented in Figure 9a. This plot shows the raw load and DCPD voltage as a function of time (LT rolling direction, air, T= 27° C). To determine the point of crack initiation, two construct lines from the DCPD data were used: one that represents the baseline DCPD data (decreasing slope) and a second that represents crack propagation (increasing slope). The intersection of these lines is the initiation point. In Figure 3a initiation occurred at  $t = 7830$  s and a load of 7810 N. From these data and the equations in ASTM E-1820 fracture toughness (K) was calculated (Figure 9b). At  $t = 7830$  we define the initiation fracture toughness  $K_i$ . For values greater than  $K_i$  crack propagation occurs. Similarly, for values less than  $K_i$ , propagation ceases. Here,  $K_i$  was equal to  $54 \text{ MPa}\cdot\text{m}^{1/2}$ . Also in Figure 9b we have calculated crack growth ( $\Delta a$ ) from the DCPD data. As can be seen in this figure the total crack growth during the rising load displacement experiment was approximately 1.5 mm. While it was noted in all experiments that for K greater than some value crack growth rate decreased, we believe this to be an artifact of the specimen size. The ASTM plane strain requirement for fracture toughness specifies that sample dimension B (Fig. 2) should be greater than  $2.5(K/\sigma_{ys})^2$ . For SS 316L this would mean testing a sample that had thickness of 7.2 cm. Due to load frame and load cell limitations,

this dimension would be impractical to test. For example, here the load required to initiate cracking was 7800 N (1755 lbs). If this value increases linearly with thickness the required load would be 55,000 N. As it relates to K, it is likely that for  $K > 70 \text{ MPa}\cdot\text{m}^{1/2}$  we do not meet the ASTM plane strain requirement and, as a result the calculated K at the crack front is higher than the actual value. This is consistent with the large crack tip opening displacement observed at the crack tip.

Here we report the  $J_{ic}$  values where the plastic contribution was calculated from the area under the load (P) crack tip opening displacement (CTOD) curve using the method for CT specimens described in ASTM E1820. A summary of  $J_{ic}$  for air, DI water, and the  $\text{MgCl}_2/\text{NaCl}$  (2 M  $\text{Cl}^-$ ) simulated crack tip solution is presented in Table 4. Also presented in Table 4 are the corresponding crack velocities (at  $J_{ic}$ ). As seen in Table 4, a decrease in  $J_{ic}$  is observed in the simulated crack tip solution as compared to air and DI water. Scanning electron micrographs of the fracture surfaces created in air and simulated crack tip solution are presented in Figures 5a and 5b. As seen in these micrographs, the air fracture surface is typical of ductile fracture. In comparison, the fracture surface created in the simulated crack tip solution is considerably less ductile. While these results indicate that the material is susceptible to SCC in this environment, the decrease in  $J_{ic}$  is small. Additional crack tip solutions and temperatures are being planned in future experiments to determine the range of  $J_{ic}$  anticipated in 3013 environments.

As it relates to 3013 and failure due to environmental fracture, these experiments are but one step in identifying crack tip solutions that may lower J. Currently we are examining the influence of low pH, other anions (such as  $\text{F}^-$ ), and increased temperature. Temperature is of particular concern as radioactive decay may result in internal temperatures in excess of  $100^\circ \text{C}$ . It has been shown for 3XX series austenitic alloys that susceptibility to SCC increases dramatically above  $60^\circ \text{C}$ .(16)

#### **LEAK BEFORE BREAK; GE/EPRI ANALYSIS FOR A CIRCUMFERENTIAL THROUGH-WALL CRACK UNDER TENSION**

##### Analytical Approach

The potential for environmental fracture of the 3013 containers raises the concern of catastrophic failure. To assess the potential for catastrophic failure we have adopted the decades old leak before break approach, that is, can we rely on the discovery of a leak (e.g. owing to through wall pitting) prior to catastrophic failure that might result from environmental fracture. One such methodology for evaluating leak before break is the GE/EPRI method developed by Kumar and German.(17, 18) The GE/EPRI method identifies the system properties (material properties, geometry, stress state, etc.) that contribute to crack extension. This method is based on a compilation of three dimensional finite element solutions for through-wall cracks in pipes (cylinders) under internal pressure. The GE/EPRI method is valid for a materials that obey the Ramberg-Osgood relationship:

$$\frac{\varepsilon}{\varepsilon_0} = \frac{\sigma}{\sigma_y} + \alpha \left( \frac{\sigma}{\sigma_y} \right)^n \quad (3)$$

where:  $\sigma$  is the stress,  $\varepsilon$  is strain,  $\sigma_y$  is the yield stress in  $N/m^2$ ,  $\varepsilon_0$  is the reference strain and is equal to  $E/\sigma_y$  where  $E$  is the modulus and is equal to  $190 GN/m^2$ , and  $n$  and  $\alpha$  are the Ramberg-Osgood coefficients. For stainless steel 316 at  $20^\circ C$   $n = 7.41$  and  $\alpha = 1.76$ . (19) GE/EPRI considers both the linear elastic and fully plastic contribution to the J-integral:

$$J_t = J_e + J_p \quad (4)$$

where  $J_e$  and  $J_p$  are the elastic and plastic components. While both axial and circumferential through wall cracks are important in 3013, here we will only consider circumferential through wall flaws. As such, for cylinders under remote tension (axial stress)  $J_e$  is defined as:

$$J_e = \frac{K^2}{E} = \frac{1}{E} \left( \frac{P_{ax} R}{2t} \right)^2 \pi a F^2 \quad (5)$$

where:  $K$  is the fracture toughness,  $P_{ax}$  is the axial load (tension) in  $N/m^2$ ,  $t$  is the cylinder wall thickness and is equal to  $1.6 \times 10^{-3} m$ ,  $R$  is the inside radius of the cylinder plus half the wall thickness and is equal to  $5.74 \times 10^{-2} m$ ,  $a$  is the crack half width assumed to be equal to the radius of a through wall pit ( $1.6 \times 10^{-3} m$ ), and  $F$  is a geometric function described below. The plastic component is defined as:

$$J_p = \alpha \sigma_y \varepsilon_0 \left( a \left( 1 - \pi/\theta \right) \right) h_1 \left( \frac{P_{ax}}{P_o} \right)^{n+1} \quad (6)$$

where:  $\theta$  is the crack angle and is equal to 0.0268 radians and  $h_1$  is another geometric function described below.  $P_o$  is the axial load limit in  $N$  and is obtained by correcting the general expression of Miller (20) for penetrating circumferential defects under pressure for the axial component of the load:

$$P_o = 2\sigma_y R t \left[ \pi - \theta - 2 \sin^{-1} \left( \frac{1}{2} \sin \theta \right) \right] \quad (7)$$

and is calculated to be 116 N.

#### Measurement of Residual Stress

Given the pressurization limits anticipated in the 3013 container (200 psi) residual stress represents the largest load on the container and the weld region is the area of largest residual stress. To measure the residual stress due to residual stress we have used the laser contour method developed by Prime *et al.* (21) In this method the area of interest is sectioned using EDM machining. This method for

sectioning is used as it does not introduce additional stress into the material. Once sectioned, stresses normal to the cutting plane result in an elastic relaxation and expansion of the cut ends (displacement of the cutting plane) the amount of which is proportional to the residual stress. This displacement is measured using a laser contour mapping technique. A finite element method is then used to calculate the normal stress the required to force the expanded material back into the cutting plane. The result is a map of residual stresses normal to the sectioning plane.

In order to improve accuracy of our stress map in the region of interest in the 3013 container, a 5 cm tall section containing the inner lid was sectioned normal to the weld using wire electric discharge machining. The displacements that resulted from this cut were between -0.025 mm and +0.025 mm. The results of the finite element analysis for residual stress are shown in the form of a stress map in Fig. 12. The large but thin-walled structure causes some difficulty in the measurements, which made for a relatively high uncertainty at about  $\pm 45$  MPa. Nevertheless, the measurements clearly found tensile stresses (hoop stress,  $\sigma_h$ ) on the order of 135-180 MPa in the weld regions; at the bottom below the joint between the lid and the cylinder wall. Similar tensile stresses are found in the bend region of the lid, presumably arising from plastic deformation during forming.

#### Construction Of The J-Integral Diagram

The original GE/EPRI tabulation of the dimensionless geometry functions  $F$  and  $h_1$  were derived for relatively small diameter thick wall vessels ( $R/t < 20$ ) as compared to the thin wall large diameter 3013 geometry ( $R/t = 37.4$ ). To overcome this limitation have used the Ji et. al. (22) tabulations for thin walled large diameter cylinder ( $R/t = 30$  and  $R/t = 40$ ) to calculate  $F$  and  $h_1$  functions for our geometry. In this method we fit the Ji et. al.  $F$  tabulations for  $R/t = 30$  and  $R/t = 40$  to third order polynomial expressions and then extrapolated these to  $a/b = 0.01$ . We then interpolated between these two values at  $a/b = 0.01$  for  $R/t = 37.4$ . A similar method was used to calculate a value for  $h_1$  for a Ramberg-Osgood coefficient  $n = 7.41$ . As such we find for a through-wall circumferential crack in the 3013 container that  $F = 0.719$  and  $h_1 = 9.97$ . With these parameters  $J_t$  was calculated from Eq. 4-6. The J-intergral results for a through-wall crack in a 3013 container under tension (axial stress) are presented in Fig. 13 as a function of normalized load. For reference we also present  $J_{1c}$  as determined from our laboratory fracture toughness experiments, the residual stress associated with the weld and a nominal pressurization of 200 psi. Assuming that the axial stress that results from the weld is equal to one half of the hoop stress ( $\sigma_{ax} = \sigma_h / 2$ ) and our laboratory measurement of  $J_{1c}$  is accurate, one would conclude from this diagram that a thorough wall penetration may not precede crack propagation. That is, because the energy to propagate a crack ( $J_{1c}$ ) for SS 316 in the NaCl/MgCl<sub>2</sub> solution is less than the energy associated with the weld residual stress. However, given the slope of the curve errors in our measurement of  $J_{1c}$  or our assumptions the  $\sigma_{ax} = \sigma_h / 2$  may change this conclusion.

In addition to these limitations, we have omitted several factors that would increase  $J_t$  for any given  $P_{ax}/P_o$ . Specifically, we have not

considered the proximity of the lid and the high degree of constraint associated with our CT experiment and resulting measurement of  $J_{1c}$  (crack face loading). The close proximity of the lid to the weld changes our assumption about the axial stress and may result in a bending moment as described by Roark.(23) In addition, the low constraint associated with a crack in a thin walled cylinder means that our laboratory CT data for  $J_{1c}$  may accurately represent the low stress triaxiality in the vicinity of the crack tip. To account for this difference in constraint weigh functions, so called T-stress, are commonly used.(24, 25) Future modifications of our model will include both end-cap effects on axial stress and bending as well as T-stress weighting functions to account for constraint.

### SUMMARY

This paper has summarized our efforts to assess corrosion related failure in stainless steel long-term storage containers baring plutonium oxides and electrorefining salts. The salts are typically composed of 95% by weight of an equimolar mixture of sodium chloride and potassium chloride with 5% by weight of anhydrous magnesium chloride. Pitting corrosion of the internal can wall is believed to occur when these salt particles deliquesce forming the electrolyte necessary for corrosion-electrochemistry. Coupon studies of stainless steel samples exposed to a Pu oxide/salt mixture for approximately 170 days found two distinct distributions; one distribution of small diameter pits in the headspace (gas) region and another in the oxide/salt contact region. Using GEV statistics these distribution were extrapolated to a benchmark storage time of 50 yrs. For the headspace region the probability of failure owing to a through-wall corrosion pit is low, the maximum pit depth after 50 yrs. being 0.26 mm. However, for the contact region the probability of a through-wall corrosion pit is finite. Our extrapolations found that the maximum pit depth after 50 yrs. would be on the order of 1.7 mm where as the container wall is only 1.6 mm thick.

To assess the susceptibility of the inner 3013 container to environmental fracture, we have measured the fracture toughness for SS 316L in air, deionized water, and a solution of  $MgCl_2/NaCl$  (2 M  $Cl^-$ ; to simulate the solution that may be present at the crack tip). Fracture toughness values ( $J_{1c}$ ) for SS316L in air was on the order  $46 \text{ kJ/m}^2 \pm 9.5$ . In comparison,  $J_{1c}$  for SS 316L in the  $MgCl_2/NaCl$  simulated crack tip solution were  $20.5 \text{ kJ/m}^2 \pm 9$ . Examination of the fracture surfaces reveals that the mechanism in air and water was largely ductile fracture. In comparison, fracture surfaces from experiments conducted in the  $MgCl_2/NaCl$  simulated crack tip solution appeared to be less ductile in nature.

Fracture toughness data from CT experiments were used in conjunction with a J-integral diagram constructed using the GE/EPRI method for linear elastic-plastic materials. As a part of this analysis the residual stress associated with the weld was measured using the laser contour method. The hoop stress in the weld region was found to be on the order of 135 MPa-180MPa. Assuming that the axial stress that results from the weld is equal to one half of the hoop stress ( $\sigma_{ax} = \sigma_h/2$ ) and our laboratory measurement of  $J_{1c}$  is accurate, one would conclude there is sufficient energy in associated with the weld to propagate a crack in the 3013 container.

## ACKNOWLEDGEMENTS

The Los Alamos National Laboratory is operated by Los Alamos National Security LLC for the National Nuclear Security Administration of the U.S. Department of Energy under contract DE-AC52-06NA25396. The authors thank Max Martinez, Ron Livingston, Jon Duffey and Poh-Sang Lam for their technical expertise and assistance. The support of Richard Mason, Kerry Dunn, GD Roberson, Allen Gunter and the 94-1 MIS Working Group is also acknowledged.

## REFERENCES

---

1. "Criteria for preparing and packaging plutonium metals and oxides for long-term storage," report no. DOE-STD-3013-2004, Department of Energy,
2. L. Avens and P. Eller, *Los Alamos Science*, **26** (2000): p. 436.
3. E. Gacria, O. Gillespie, S. Joyce, D. Veirs and L. Worl, "Deliquescent behavior of  $\text{KMgCl}_3$ ,  $\text{K}_2\text{MgCl}_4$ ,  $\text{K}_3\text{NaMgCl}_6$ , and electrorefining salt," report no. LA-UR-07-4356, Los Alamos National Laboratory, 2007.
4. L. Greenspan, *Journal of Research of the National Bureau of Standards - A. Physics and Chemistry*, **81A** (1977): p. 89-96.
5. Y. Marcus and N. Soffer, *J. Chem. Soc., Faraday Trans.*, **84** (1988): p. 3575-3585.
6. R. T. Pabalan, L. Yang and L. Browning, *Mat. Res. Soc. Symp. Proc.*, **713** (2002): p.
7. M. A. Hill and R. S. Lillard, *Corrosion*, **62** (2006): p. 801.
8. P. J. Laycock, R. A. Cottis and P. A. Scarf, *Journal of the Electrochemical Society*, **137** (1990): p. 64.
9. J. R. M. Hosking, *Applied Statistics*, **34** (1985): p. 301.
10. "Standard Test Method for Measurement of Fracture Toughness," report no. Designation E 1820-01, ASTM International, 2001.
11. D. Kolman, *Corrosion Science*, **43** (2001): p. 99-125.
12. R. C. Newman and A. Mehta, in *Environment-Induced Cracking of Metals, NACE-10*, R. Gangloff and M. Ives, Ed., p. 489, (1988).
13. G. Odette, P. Maziasz and J. Spitznagel, *Journal of Nuclear Materials*, **103-104** (1981): p. 1289.
14. S. Maloy, M. James, G. Willcutt, W. Sommer, M. Sokolov, L. Snead, M. Hamilton and F. Garne, *Journal of Nuclear Materials*, **296** (2001): p. 119.
15. Y. Matsui, M. Niimi, T. Hoshiya, F. Sakurai, S. Jitsukawa, T. Tsukada, M. Ohmi, H. Sakai, R. Oyamada and T. Onchi, *Journal of Nuclear Materials*, **233-237A** (1996): p. 188.
16. A. Sedriks, *Corrosion of Stainless Steels*, p. 299, A. Wiley-Interscience, New York (1996).
17. V. Kumar, M. German and C. Shih, "An Engineering Approach for Elastic-Plastic Fracture Analysis," report no. NP-1931, EPRI, 1981.
18. V. Kumar, M. German, W. Wilkening, W. Andrews, H. deLorenzi and D. Mowbray, "Advances in Elastic-Plastic Fracture Analysis," report no. NP-3607, EPRI, 1984.
19. Y. Kim, N. Huh, Y. Kim, Y. Choi and J. Yang, *Journal of Pressure Vessel Technology*, **126** (2004): p. 277.
20. A. Miller, *International Journal of Pressure Vessels & Piping*, **32** (1988): p. 197.

21. M. B. Prime, *Journal of Engineering Materials and Technology*, **123** (2001): p. 162.
22. W. Ji, Y. Chao, M. Sutton, P. Lam and G. GE Mertz, "*J-integral of circumferential crack in large diameter pipes*," in Proceedings of the 2nd ASME-JSME Nuclear Engineering Joint Conference, 1993 (ASME-JSME), p. 139.
23. W. Young, *Roark's Formulas for Stress and Strain*, p. McGraw-Hill, New York (2002).
24. J. Rice, *Journal of Mechanical Physics and Solids*, **22** (1974): p. 17.
25. T. Lewis, X. Wang and R. Bell, "*Finite Element Analysis of Circumferential Cracks in Thin Walled Cylinders: T-Stress Solutions*," in Proceedings of IPC 2006, 2006 (ASME).

TABLE 1

Properties and composition of ARF223-SSR110 Pu oxide/salt mixture.

Density - Bulk pycnometer	6.7	g/cm <sup>3</sup>
Specific Surface Area	0.5	m <sup>2</sup> /g
Specific Power (W / kg-net)	1.76	W/kg
Pu	648.3	g
Pu	70.2	wt. %
Carbon	0.15	wt. %
Calcium	0.03	wt. %
Chromium	0.12	wt. %
Chloride	5.50	wt. %
Copper	0.01	wt. %
Gallium	0.06	wt. %
Iron	0.06	wt. %
Fluoride	0.06	wt. %
Potassium	1.87	wt. %
Magnesium	0.54	wt. %
Manganese	0.01	wt. %
Sodium	1.47	wt. %
Nickel	0.27	wt. %
Phosphorus	0.01	wt. %
Silicon	0.07	wt. %
Sulfur	0.03	wt. %

TABLE 2

Partial pressures (kPa) in ARF223-SSR110 obtained from GC analysis and total pressure. Pressure increases seen in CO<sub>2</sub>, CO, and H<sub>2</sub> while O<sub>2</sub> is being depleted.

Date	partial pressures, kPa		
	04/09/03	04/17/03	08/19/03
CO2	1.0	1.4	9.0
N2O	0.1	0.2	0.3
He	58.3	60.3	57.6
H2	0.7	1.0	4.2

O2	8.6	1.5	0.4
N2	43.7	43.4	44.4
CH4	0.0	0.1	0.2
CO	0.5	0.6	3.8
Total Pressure	112.7		108.4

TABLE 3  
Fitting Parameters from GEV analysis of pit depths.

	$\alpha$	$k$	$u$
headspace	3.513	-0.1032	13.73
contact region	7.993	-0.5182	13.90

TABLE 4  
Values for  $J_c$  from CT experiments.

	air	DI water	Na/Mg-Cl (2 M Cl <sup>-</sup> )
$J_c$ (ASTM E1820)	46.0±9.5 kJ/m <sup>2</sup>	36.0±5 kJ/m <sup>2</sup>	20.5±9.0 kJ/m <sup>2</sup>

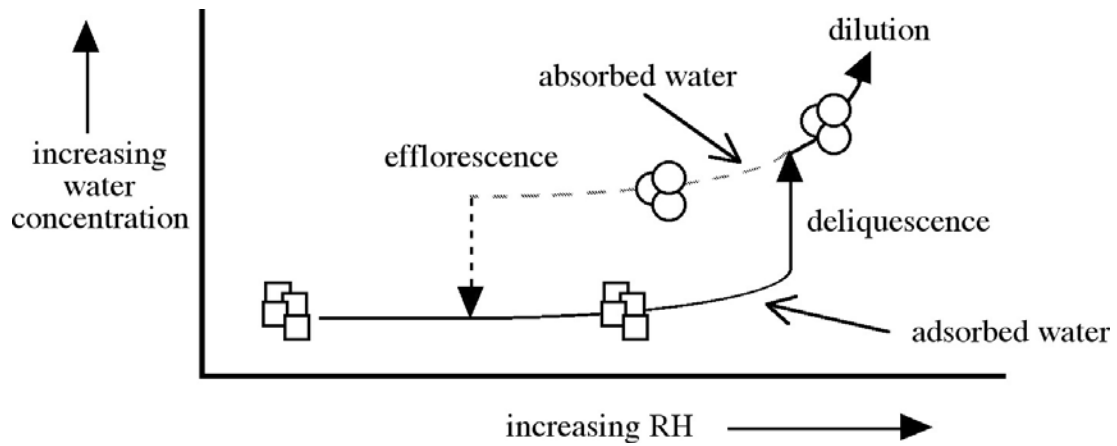


FIGURE 1 - Diagram depicting the relationship between salt water content, relative humidity, and deliquescence.

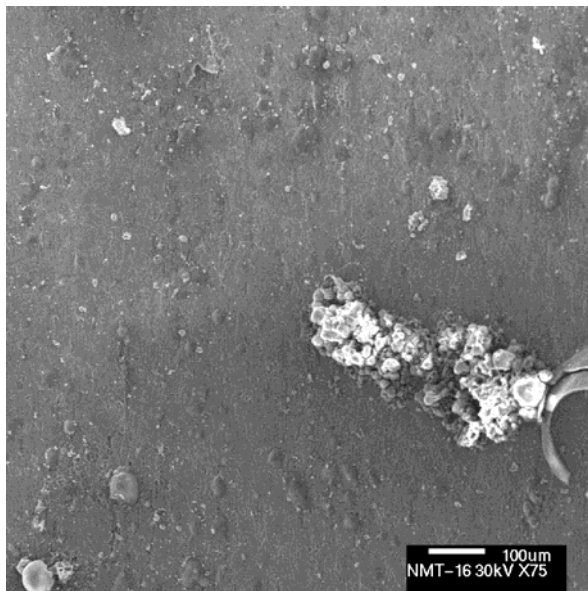


Figure 2a - Surface of ARF223-SSR110 after exposure but before cleaning.

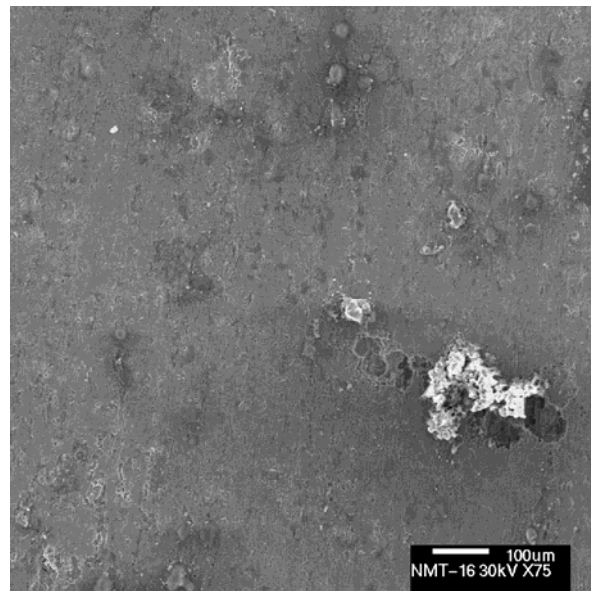


Figure 2b - Surface of ARF223-SSR110 after exposure and cleaning. Same are as 2a.

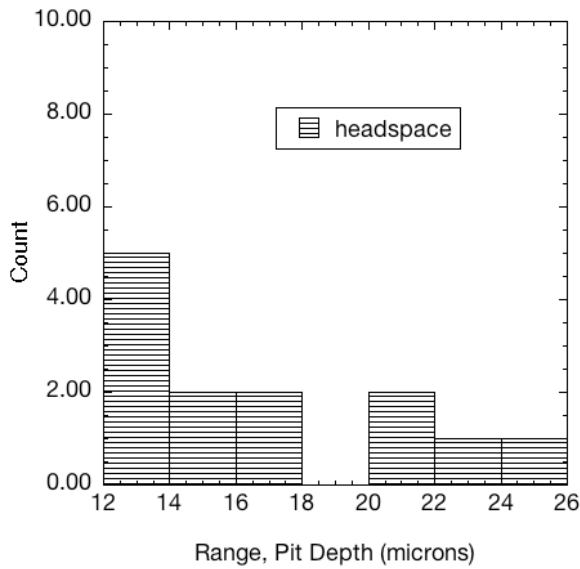


Figure 3 - Histogram showing distribution of pit depths in the headspace region of ARF223-SSR110.

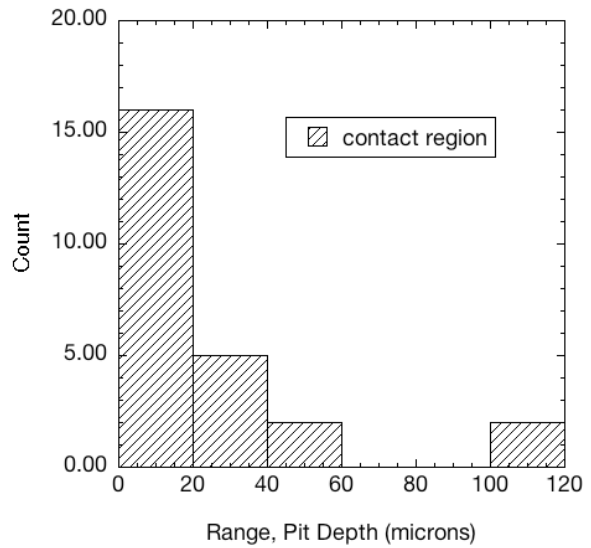


Figure 4 - Histogram showing distribution of pit depths in the oxide/salt contact region of ARF223-SSR110.

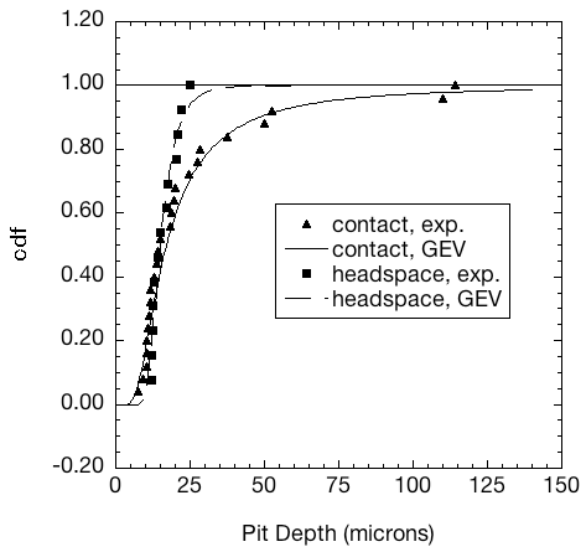


Figure 5 - Cumulative distribution and GEV fit to pit depths in headspace and contact regions of ARF223-SSR110.

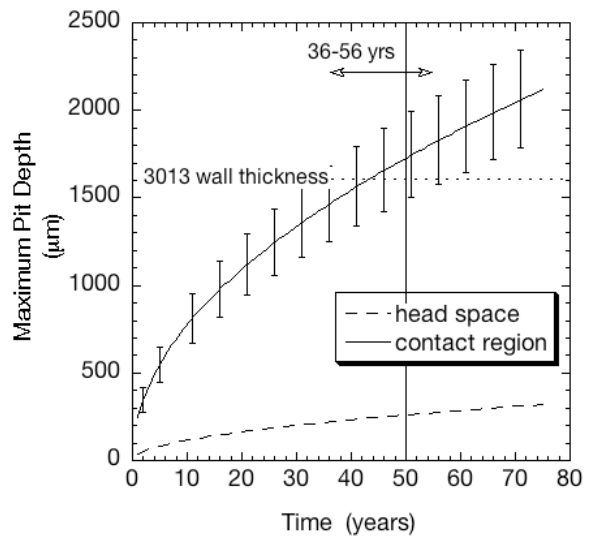


Figure 6 - GEV extrapolation in space and time for pit depths in headspace and contact regions of ARF223-SSR110.

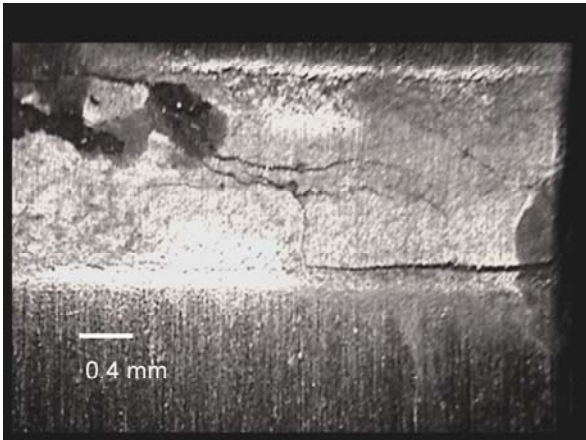


Figure 7a - Environmental fracture observed after exposure of a teardrop specimen to a Ca rich Pu oxide/ER salt mixture. Weld region.

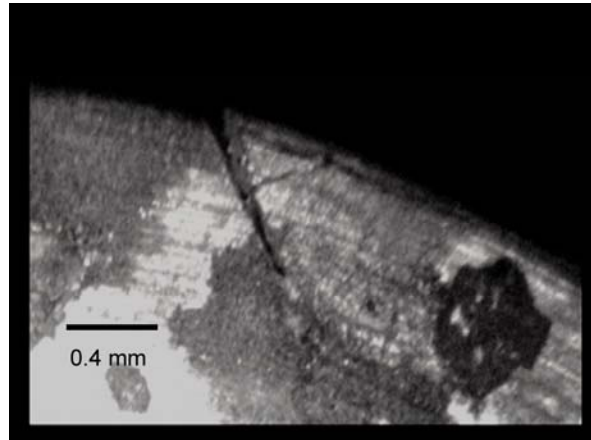


Figure 7b - Environmental fracture observed after exposure of a teardrop specimen to a Ca rich Pu oxide/ER salt mixture. Edge view of 7a.

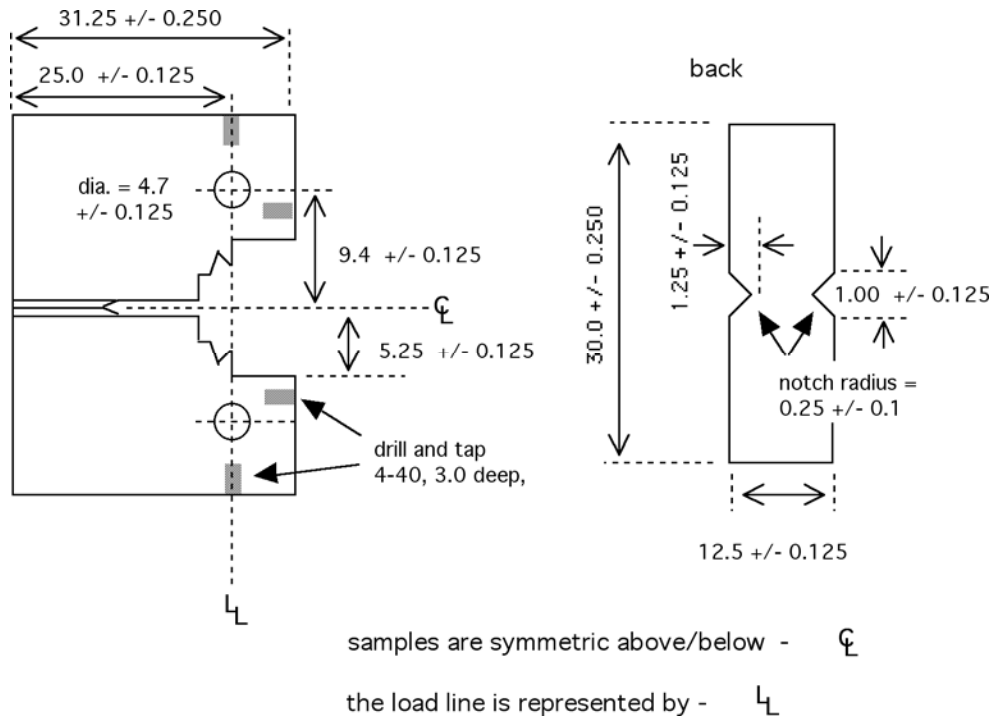


Figure 8 - Diagram of CT specimens used in the fracture toughness

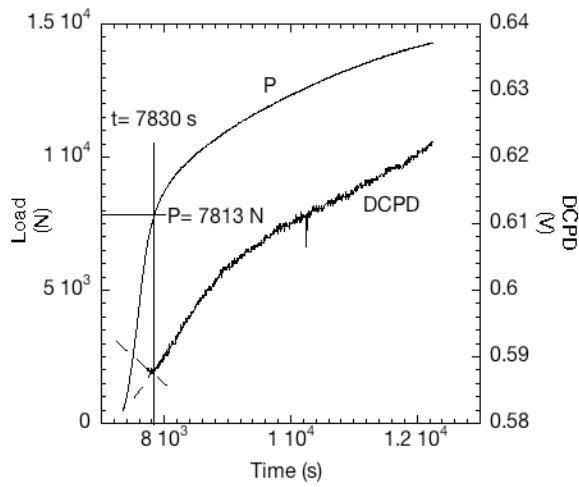


Figure 9a - Rising load displacement data for SS 316 in air.

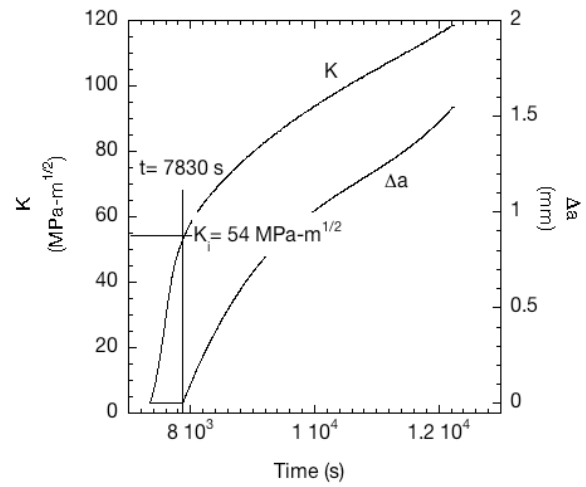


Figure 9b - Calculation of fracture toughness and crack growth from data in 9a.

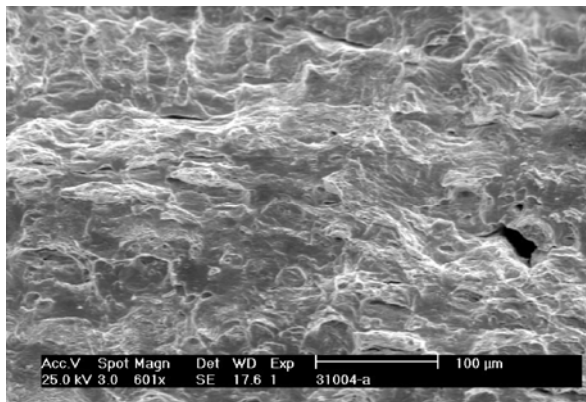


Figure 10a - Surface of a CT specimen after fracture in air.

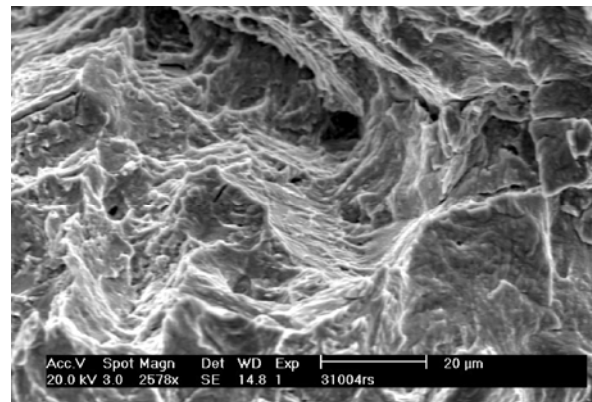


Figure 10b - Surface of a CT specimen after fracture in NaCl/MgCl<sub>2</sub> (2 M Cl<sup>-</sup>) solution.

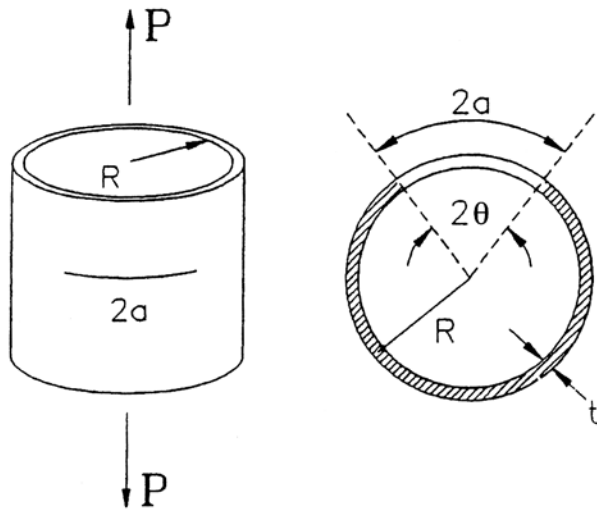


Figure 11 - Diagram depicting the geometric parameters referred to in the GE/EPRI analysis.

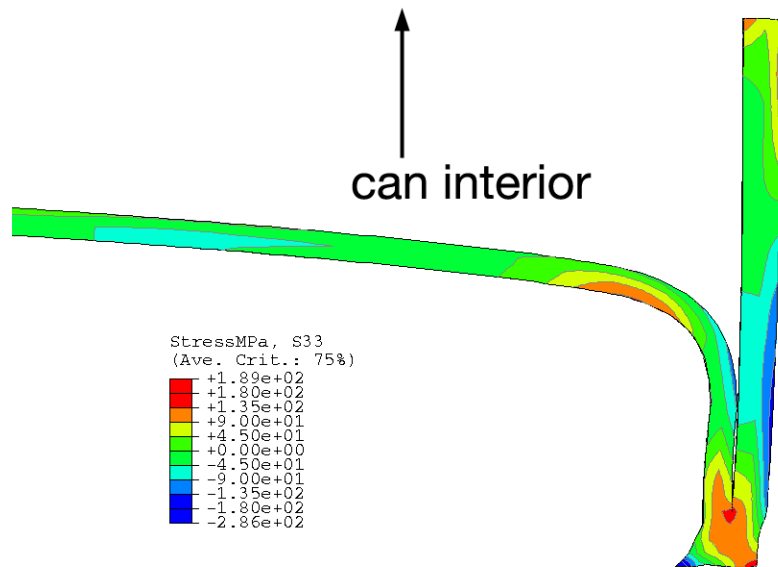


Figure 12 - Residual stress map of a section of the 3013 can lid. Can interior and bottom are towards the top of the figure.

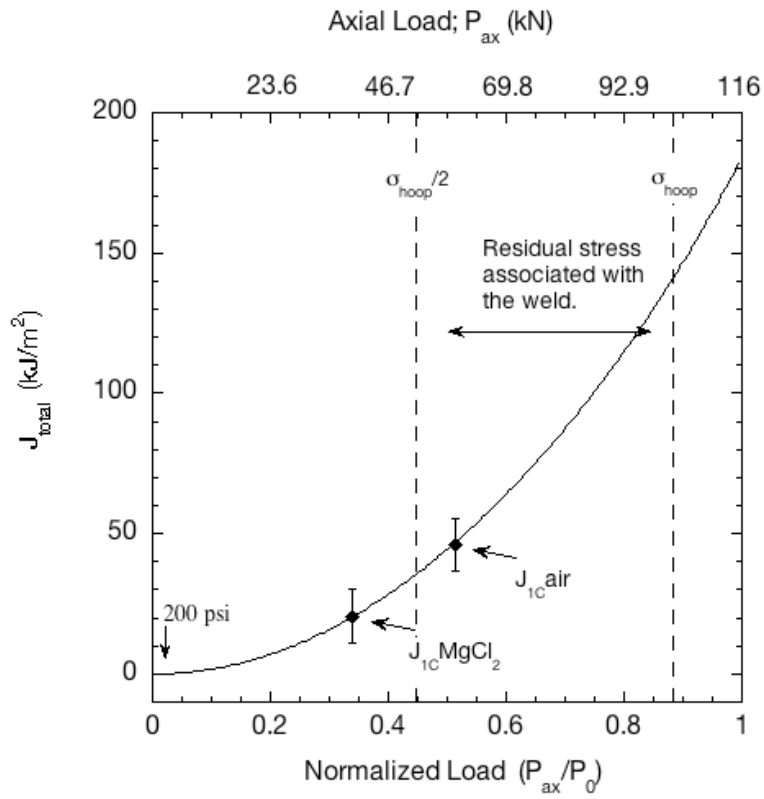


Figure 13 - J-integral diagram for a 3013 inner container with a 1.6 mm flaw constructed using the GE/EPRI method.